

The IACOB project

XVI. Surface helium abundances in Galactic O-type stars: indications for identifying binary interaction products

S. Simón-Díaz^{1,2}, G. Holgado^{1,2}, C. Martínez-Sebastián^{1,2}, M. Carretero-Castrillo^{3,4}, H. Jin⁵, M. A. Urbaneja⁶, R. Gamen⁷, J. Puls⁸, A. de Burgos⁴, M. García⁹, A. Herrero^{2,1}, Z. Keszthelyi¹⁰, N. Langer^{5,11}, F. Najarro⁹, J. M. Paredes³, M. Ribó³

¹ Instituto de Astrofísica de Canarias, E-38200 La Laguna, Tenerife, Spain.

² Departamento de Astrofísica, Universidad de La Laguna, E-38205 La Laguna, Tenerife, Spain.

³ Departament de Física Quàntica i Astrofísica, Institut de Ciències del Cosmos (ICCUB), Universitat de Barcelona (IEEC-UB), c. Martí i Franquès, 1, 08028 Barcelona, Spain

⁴ European Southern Observatory, Alonso de Córdova 3107, Vitacura, Santiago, Chile

⁵ Argelander Institut für Astronomie, Auf dem Hügel 71, DE-53121 Bonn, Germany

⁶ Universität Innsbruck, Institut für Astro- und Teilchenphysik, Technikerstr. 25/8, A-6020 Innsbruck, Austria

⁷ Instituto de Astrofísica de La Plata, Facultad de Ciencias Astronómicas y Geofísicas, CONICET-UNLP, Paseo del Bosque s/n, La Plata, Argentina.

⁸ LMU Munich, Universitätssternwarte, Scheinerstrasse 1, 81679 München, Germany

⁹ Centro de Astrobiología, CSIC-INTA, Crtra. de Torrejón a Ajalvir km 4, 28850 Torrejón de Ardoz (Madrid), Spain

¹⁰ School of Mathematics, Statistics and Physics, Newcastle University, UK

¹¹ Max-Planck-Institut für Radioastronomie, Auf dem Hügel 69, DE-53121 Bonn, Germany

Date

ABSTRACT

Context. The presence of massive O-type stars with surfaces enriched by CNO-cycle products has been known since the early 1980s. For many years, internal rotational mixing was assumed to be the dominant mechanism responsible for this chemical contamination. However, accumulating evidence now suggests that binary interaction – particularly mass-transfer episodes – may play an equally important, if not dominant, role.

Aims. To carry out a large-scale investigation of surface helium (He) abundances in Galactic O-type stars, based on the results from the analysis of high-quality spectroscopic data from the IACOB project.

Methods. We perform a homogeneous spectroscopic analysis of 318 Galactic O-type stars with the IACOB-BROAD and FASTWIND/IACOB-GBAT tools, deriving rotational velocities, atmospheric parameters, and He abundances. We also account for the influence of binarity, runaway status, and parameter degeneracies (e.g., microturbulence, wind properties, diagnostic lines, and companion contamination) on the abundance determinations.

Results. We present homogeneously determined surface He abundances ($Y_{\text{He}} = N_{\text{He}}/N_{\text{H}}$) for the so far largest, statistically significant sample of Galactic O-type stars. About 78% of the stars show He abundances consistent with the previously proposed cosmic abundance standard of $Y_{\text{He}} = 0.098 \pm 0.002$. The remaining 22% display clear He enrichment ($Y_{\text{He}} \gtrsim 0.13$). We also provide observational evidence indicating that most of these He-enriched stars are likely the products of binary interaction.

Conclusions. Our study highlights how large spectroscopic surveys are gradually opening robust observational avenues to identify the products of massive binary interaction. It also emphasizes the need for caution when interpreting the spectroscopic properties of apparently single O-type stars. A significant fraction may in fact be the outcome of binary evolution rather than isolated stellar birth.

Key words. Stars: early-type – Stars: massive – Stars: abundances – Stars: rotation – Techniques: spectroscopic – binaries: general

1. Introduction

The seminal paper by Herrero et al. (1992) presented the results of a spectroscopic analysis of 25 Galactic O-type stars using plane-parallel, hydrogen+helium, non-LTE stellar atmosphere models. Using mid-resolution spectra covering the 4000–5000 Å range, they reported that more than 60% of the stars exhibited helium (He) abundances higher than the cosmic standard. This result was unexpected given the state-of-the-art understanding of stellar interiors and evolution at the time (e.g.,

Maeder 1990): the existence of a large radiative zone surrounding the convective core of a massive main sequence star was avoiding that elements generated in the core during hydrogen burning could reach the external layers of the star.

Most of the enriched stars were either fast rotators or objects with low surface gravities and high luminosities – that is, those classified as Ia, Iab, or displaying the f and (f) qualifiers (see, e.g., Sota et al. 2011) – indicating that, from a single-star evolutionary perspective, they had already evolved significantly away from the zero-age main sequence (ZAMS). This inconsistency between the abundances resulting from the spectroscopic analyses and theoretical predictions became widely known as the *he-*

lum discrepancy problem (Herrero et al. 1992). Moreover, these findings were consistent with earlier pioneering works by Walborn (1970, 1971, 1976), Kudritzki et al. (1983), Bohannan et al. (1986), Voels et al. (1989), and Schonberner et al. (1988), which had already reported stars not only with helium-enriched surfaces, but also with carbon, nitrogen and oxygen (CNO) abundance patterns indicative of CNO-cycle processing – namely, simultaneous enrichment in helium and nitrogen, depletion of carbon, and nearly normal oxygen.

Maeder (1987) (see also Langer 1992, and references therein) proposed that turbulent diffusion in the radiative zones of massive main-sequence stars, potentially triggered by differential rotation, could lead to a significant redistribution of elements during the core hydrogen burning phase. This mechanism offered a plausible explanation for the detection of stellar surfaces enriched in CNO-cycle products. Building upon this idea, a new generation of stellar interior models was developed to incorporate the effects of rotation on the evolution of massive stars (see the review by Maeder & Meynet 2000). These models (e.g., Heger & Langer 2000; Brott et al. 2011; Ekström et al. 2012) aimed not only to reproduce the observed surface abundance patterns, but also to address several other discrepancies between earlier theoretical predictions and observations, including the so-called *mass discrepancy problem* (Groenewegen et al. 1989; Herrero et al. 1992).

Several observational studies of small- to medium-sized samples of O- and B-type stars in different metallicity environments soon followed (e.g., Herrero et al. 1999, 2000; Repolust et al. 2004; Mokiem et al. 2005; Hunter et al. 2009; Przybilla et al. 2010; Rivero González et al. 2012; Bouret et al. 2012, 2013, 2021; Martins et al. 2015a,b, 2016, 2017, 2018; Proffitt et al. 2016, 2024; Grin et al. 2017; Cazorla et al. 2017; Markova et al. 2018; Dufton et al. 2018, 2020). Contrary to the expectations, these works provided growing empirical evidence that rotational mixing may not be the sole – or even the dominant – mechanism responsible for the appearance of CNO-cycle products at the surfaces of massive main-sequence stars. The detection of a non-negligible fraction of slowly rotating stars (as measured by projected rotational velocities, $v \sin i$) whose surfaces were nonetheless clearly N-enriched was one of the most challenging results (e.g., Morel et al. 2008; Hunter et al. 2008, for the first statistically significant evidence of the challenge).

Some of the solutions proposed to reconcile theory with observations are: improved treatments of internal angular momentum transport and convective boundary mixing (Maeder et al. 2014; Simoniello et al. 2015); a reassessment of the accuracy and reliability of spectroscopically derived abundances (Maeder et al. 2014); the influence of magnetic fields (e.g., Keszthelyi et al. 2019, 2020); and the inclusion of additional transport mechanisms such as internal gravity waves (e.g., Aerts et al. 2014; Brinkman et al. 2025; Mombarg et al. 2025). Another scenario that is gathering increasing observational support is the role of binary interaction, in particular through mass-transfer episodes (e.g., Vanbeveren 1988, 1993; de Mink et al. 2009; Song et al. 2018; Richards et al. 2024; Jin et al. 2025).

Surface N (plus C and O) abundances, together with $v \sin i$, have been the main observational diagnostics used so far to test the efficiency of rotational mixing and to evaluate alternative scenarios proposed to explain the observed empirical patterns (see references above). In that regard, the pioneering works by Proffitt et al. (2016, 2024), who used boron abundance estimates derived from the quantitative spectroscopic analysis of UV spectra obtained with the Hubble Space Telescope Cosmic Origins Spectrograph (see also the theoretical predictions by Frischknecht

et al. 2010). They detected partial depletion of boron at a level consistent with that expected for rotational mixing in single stars, but inconsistent with expectations for depletion from close binary evolution (see also Jin et al. 2024a). Their results also suggest that the efficiency of rotational mixing is at or slightly below the low end of the range predicted by the available theoretical calculations.

Despite helium was the first element to highlight the need for improved theories of stellar evolution (Herrero et al. 1992), studies specifically dedicated to its determination and use remain remarkably scarce (e.g., Herrero et al. 2000; Repolust et al. 2004; Mokiem et al. 2005; Martins et al. 2015a; Markova et al. 2018; Aschenbrenner et al. 2023). This is partly due to the intrinsic complexity of deriving reliable He abundances (particularly in B-type stars, but also in O-type; see, e.g., Villamariz & Herrero 2000; Villamariz et al. 2002). In addition, the relatively high baseline abundance and slow surface enrichment timescale of He makes it considerably more difficult to detect surface variations compared to other elements, further limiting its widespread usage as an observational diagnostic.

In this paper, motivated by the results of Martínez-Sebastián et al. (2025), who pointed to the potential of He abundances as a key diagnostic to identify candidate binary interaction products (BIPs), we embark on the first large-scale investigation of surface He abundances in Galactic O-type stars. Our study is based on the analysis of a high-quality spectroscopic dataset assembled within the framework of the IACOB project Simón-Díaz et al. (2011, 2015, 2020). This work continues the efforts initiated in Holgado et al. (2018, 2022) and Martínez-Sebastián et al. (2025), and is complemented by a parallel study of surface nitrogen abundances (Martínez-Sebastián et al., subm.).

The structure of the paper is as follows. The description of the working sample and observational material is provided in Sect. 2, while Sect. 3 concentrates on the methodology used to obtain estimates of projected rotational velocities, atmospheric parameters, and He abundances. Section 4 summarizes key results of our investigation, including the general distribution of He abundances, comparison with results from the literature, and the distribution of the stars in the Hunter and spectroscopic Hertzsprung–Russell diagrams (Hunter et al. 2008; Langer & Kudritzki 2014), and the analysis in runaway and binary status. A discussion of the results, our main conclusions, and future prospects are presented in Sects. 5 and 6.

2. Sample description

The sample considered in this work comprises 318 Galactic O-type stars with at least one high-resolution spectrum available in the IACOB spectroscopic database (most recently described in Simón-Díaz 2020), and which fulfill the following criteria: (1) they have not been identified as clear double-lined or higher-order spectroscopic systems; (2) the available spectra have a signal-to-noise ratio (S/N) above 50; (3) they do not exhibit peculiar spectral features (e.g., Oe, Ope, or Of?p, see Sota et al. 2011, 2014; Maíz Apellániz et al. 2016) that affect the diagnostic lines used to determine spectroscopic parameters; (4) they have both He I and He II lines strong enough to be reliable as effective temperature indicators; and (5) they do not show a H_β line in emission (i.e. hypergiants are excluded). A few additional stars were excluded from the sample after performing the quantitative spectroscopic analysis, as briefly described in Sect. 3.

As noted elsewhere in this paper (e.g., Sect. 4), our sample densely covers the region of the Hertzsprung–Russell diagram (HRD) populated by O-type stars, all of them being located

within the main sequence (MS) band. Because no specific filtering was applied in terms of $v \sin i$ (unlike in Martínez-Sebastián et al. 2025, subm.), the resulting distribution closely resembles that presented in Holgado et al. (2020), with a main $\sim 75\%$ component of stars centered at $\sim 80 \text{ km s}^{-1}$, and an extended high-velocity tail ($v \sin i \gtrsim 200 \text{ km s}^{-1}$) reaching up to $\sim 450 \text{ km s}^{-1}$.

Among 237 of 318 stars for which we have multi-epoch spectroscopy, 73 were identified as single-line spectroscopic binaries (SB1), based either on radial velocity variations detected across all available spectra in the IACOB database (following Holgado et al. 2018; Holgado 2019; Simón-Díaz et al. 2024), or on a detailed investigation of spectroscopic binarity within the OWN survey (Barbá et al. 2010, 2017; Gamen et al. 2008, subm.). The remaining stars were classified as likely single (LS), although some may still harbor undetected companions.

Updated information on the runaway (RW) status is available for almost 85% of the stars in the sample. This is based on the studies of Maíz Apellániz et al. (2018) and Carretero-Castrillo et al. (2023, 2025), all derived from *Gaia* astrometric data (e.g. Gaia Collaboration et al. 2016, 2023). Stars for which the RW status is not available are those that did not satisfy the quality cuts established in Carretero-Castrillo et al. (2023, their Appendix A) to ensure reliable astrometric data.

As a final point of interest, our sample includes a significantly enhanced number of ON stars (19) compared with the 12 ON stars analyzed in the most recent comprehensive study of these type of objects by Martins et al. (2015b).

3. Methodology

We used the best available spectrum for each star (in terms of S/N) from the IACOB spectroscopic database¹. All spectra have a resolving power between $R = 25\,000$ and $R = 85\,000$, and typically cover the wavelength range from ~ 3900 to 9000 \AA . The mean of the S/N distribution is 150 ± 55 , with a minimum of 50, and 80% of the stars having $S/N \gtrsim 100$.

A detailed description of the analysis strategy used to derive the line-broadening and spectroscopic parameters of the sample stars is provided in Holgado et al. (2018). Briefly, we first estimated $v \sin i$ and the macroturbulent broadening (v_{mac}) using the IACOB-BROAD tool (Simón-Díaz & Herrero 2014), following the procedures outlined in Simón-Díaz & Herrero (2007, 2014) and Simón-Díaz et al. (2017). Other spectroscopic parameters, such as the effective temperature (T_{eff}), surface gravity ($\log g$), macroturbulence (ξ_t), wind-strength Q parameter² (Puls et al. 1996), and surface helium abundance ($Y_{\text{He}} = N_{\text{He}}/N_{\text{H}}$), were then determined using IACOB-GBAT (Simón-Díaz et al. 2011; Sabín-Sanjulián et al. 2014; Holgado et al. 2018).

Although a large fraction of the stars in our sample had already been analyzed in Holgado (2019, PhD thesis), there are two important updates with respect to the results presented there and in the associated papers (i.e. Holgado et al. 2018, 2020, 2022). First, we studied 117 additional stars³ for which spectra were not available at the time of those publications. Second, we reanalyzed the entire sample using an extended version of the grid of FASTWIND models (Santolaya-Rey et al. 1997; Puls et al. 2005; Rivero González et al. 2011) which was employed in Holgado et al. (2020, Table 2). Specifically designed for the purposes of this study, the new grid was computed from scratch with

¹ <https://research.iac.es/proyecto/iacob/iacobcat/>

² $Q = \dot{M}/(v_{\infty} R)^{1.5}$, with \dot{M} in $\text{M}_{\odot} \text{ yr}^{-1}$, v_{∞} in km s^{-1} , and R in R_{\odot}

³ A certain percentage of them not fulfilling the criteria described in Sect. 2, and hence excluded for the final sample under study.

Table 1: Parameter space covered by the grid of FASTWIND models at solar metallicity.

Parameter	Range	Step size	Units
T_{eff}	22 000 ... 55 000	1 000	[K]
$\log g$	2.6 ... 4.4	0.1	[dex]
ξ_t	1 ... 15	2	$[\text{km s}^{-1}]$
	15 ... 30	5	$[\text{km s}^{-1}]$
Y_{He}^{a}	0.06 ... 0.20	0.02	
	0.20 ... 0.30	0.05	
$\log Q^{\text{b}}$	-11.9 ... -12.7	0.2	[dex]
	-13.0 ... -15.0	0.5	[dex]
β	0.8 ... 1.2	0.2	

Table 2: Diagnostic lines used in the IACOB-GBAT spectroscopic analysis of our sample of Galactic O-type stars

H	He I	He II	He I + He II
$\text{H}\alpha$	$\lambda 4387$	$\lambda 4200$	$\lambda 4026$
$\text{H}\beta$	$\lambda 4471$	$\lambda 4541$	$\lambda 6678 + \lambda 6683$
$\text{H}\gamma$	$\lambda 4713$	$\lambda 4686$	
$\text{H}\delta$	$\lambda 4922$	$\lambda 5411$	
		$\lambda 5875$	

FASTWIND v10.6.5, and includes: (1) a reduced step size in Y_{He} , changed from 0.05 to 0.02, (2) a lower minimum helium abundance of 0.04, and (3) an improved sampling of microturbulence below 15 km s^{-1} (see Table 1), together with two additional grid points at 25 and 30 km s^{-1} .

Our main motivation for reanalysing the full sample with an extended grid was twofold: namely, to improve the accuracy of our He abundance estimates⁴, and to enable a more detailed investigation of a non-negligible subsample of stars for which the original grid yielded upper limits on the helium abundance of about 0.08 (further details in Sect. 5.1).

Table 1 summarizes the parameter space covered by the extended FASTWIND grid. Table 2 lists the complete set of optical hydrogen (H I) and helium (He I, He II) lines synthesized in the FASTWIND models. By default, in the IACOB-GBAT analyses, we used the full set of indicated lines, and allowed the tool to explore a broad range of values for all free parameters, except for the velocity-law exponent, which was fixed⁵ to $\beta = 1$. We also took advantage of the option to quickly recompute the best-fitting solution after excluding selected diagnostic lines or fixing specific grid parameters. This capability allowed us to assess in an objective, yet efficient, way the impact of individual lines or parameters on the derived He abundances (see Appendix A).

As in Holgado et al. (2018), both $v \sin i$ and v_{mac} were considered as fixed parameters in the default IACOB-GBAT analyses, using the values quoted in columns 3 and 4 of Tables C.1 to C.3. These values were taken directly from the outcome of the IACOB-BROAD analysis, with the exception of the v_{mac} estimates for those stars with a $v \sin i \gtrsim 200 \text{ km s}^{-1}$, in which case v_{mac} was fixed to zero.

As in previous IACOB papers, although we benefited from the ability of IACOB-GBAT to provide a more complete and objective exploration of the parameter space (compared to traditional by-eye techniques), we adopted its results with a critical view. As with any automated method, final revision by the user

⁴ See also Keszthelyi et al. (2021)

⁵ Also, the full grid was computed neglecting the impact of wind-clumping.

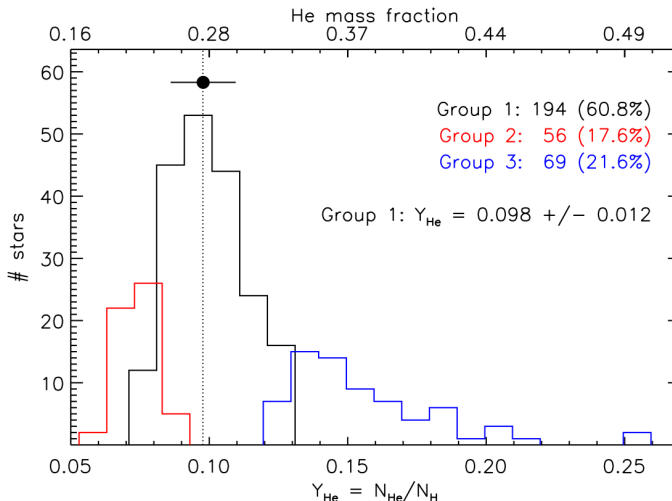


Fig. 1: He abundance distributions for the three groups of stars introduced in Sect. 4.1. Vertical dotted line indicates the present-day cosmic reference value provided by Nieva & Przybilla (2012). Black dot and horizontal line indicate mean and standard deviation associated with Group 1 stars.

was essential. We therefore performed a visual assessment of the agreement between the best-fitting model and the observed spectrum. This step allowed us to identify cases requiring adjustments, such as refining the radial-velocity correction or modifying the adopted line-broadening parameters, as well as situations in which the derived parameters were unreliable. The latter included limitations of the `FASTWIND` grid (e.g., the use of 1D unclumped models) or the misclassification of composite spectra as originating from single stars.

4. Results

Tables C.1 to C.3 summarize the relevant information of the 318 Galactic O-type stars analyzed in this study. The stars are grouped in three tables according to their classification as He-low, He-normal, or He-rich, as defined in Sect. 4.1. Within each group, stars are sorted first by spectral type (SpT) and then by luminosity class (LC), following the classifications reported in the Galactic O-Star Catalog (GOSC v4.2, Maíz Apellániz et al. 2013, 2017). For each star, we provide the adopted values of $v \sin i$ and v_{mac} (columns 3 and 4) used as input in the `IACOB-GBAT` analysis, as well as the results of the analysis (columns 5 to 9) obtained when all free parameters were allowed to vary and the full set of diagnostic lines was considered. The various tables also list the quality flag assigned from the visual assessment of the agreement between the best-fitting model and the observed spectrum (column 10), the number of spectra available to identify whether the star is a spectroscopic binary, and indicates whether the star has been identified as a SB1 (column 12) and/or a runaway (column 13).

In this paper, we primarily focus on the He abundances resulting from the `IACOB-GBAT` analysis. For a more detailed discussion of other aspects of the sample – such as their physical properties (including spin rates) and the identification of potential binary interaction products – we refer to Holgado et al. (2020, 2022); Britavskiy et al. (2023); Martínez-Sebastián et al. (2025) and Carretero-Castrillo et al. (2025).

4.1. General distribution of He abundances

Figure 1 presents the first comprehensive distribution of surface He abundances for a statistically significant sample of Galactic O-type stars analyzed homogeneously. We divide the sample into three groups using as reference the present-day cosmic abundance of He proposed by Nieva & Przybilla (2012). This reference abundance ($Y_{\text{He}} = 0.098 \pm 0.002$) was obtained from a thorough quantitative spectroscopic analysis of a carefully selected sample of early-B type stars in the Solar Neighborhood. Group 1 comprises 193 stars (~61% of the sample) whose estimated abundances are compatible – taking into account their associated uncertainties (ΔY_{He}) – with the indicated reference value. Group 2 gathers the non-negligible number of 56 stars (~18%) for which the default `IACOB-GBAT` analysis yields unrealistically low He abundances (i.e., $Y_{\text{He}} + \Delta Y_{\text{He}} < 0.098$, Sect. 5.1). Group 3 covers the 69 stars in the high He abundance tail of the distribution (~22%) clearly showing surface He enrichment compared with the reference value (i.e. $Y_{\text{He}} - \Delta Y_{\text{He}} > 0.098$). Some overlap occurs between the values of Group 1 and those of Groups 2 and 3, which arises from the individual uncertainties associated with stars whose He abundances fall in between $\sim 0.07 - 0.09$ and $\sim 0.12 - 0.13$, respectively (see Fig. 1). In this regard, we note that typical (formal) uncertainties in Y_{He} resulting from the default `IACOB-GBAT` analysis for Groups 1 to 3 are 0.025, 0.014, and 0.045 (i.e. 26, 21, and 28%), respectively. Hereafter, we will call the stars comprising these three groups He-normal, He-low, and He-rich, respectively.

4.2. Comparison with results from the literature

As in previous `IACOB` studies, we compare our results with those available in the literature. In this work, we focus on four recent studies selected because they provide abundances for at least ten stars in common with our sample: namely Repolust et al. (2004); Martins et al. (2015b); Markova et al. (2018) and Aschenbrenner et al. (2023). The first two are based on the `FASTWIND` atmosphere code, as in our study; the third employs `CMFGEN` (Hillier & Miller 1998); and the last one relies on a hybrid analysis combining `ATLAS9` atmosphere models (Kurucz 1993) with spectral synthesis calculations performed with `DETAIL` and `SURFACE` (see also Nieva & Przybilla 2012).

Figure 2 shows the outcome of this comparison, where the one-to-one relation and the 25% tolerance region are indicated as dashed and dotted lines, respectively. Taking into account the associated uncertainties, we find a reasonably good agreement for most of the (67) stars in common with any of the abovementioned studies. Nevertheless, a small subset of (14) stars shows discrepancies beyond 25%. Appendices B and A provide additional notes on these specific stars. They include a discussion of the possible origin of such discrepancies.

Complementing this exercise, we also performed a fully independent analysis of a subsample of ~ 50 of the stars under study with the code `MAUI` (Urbaneja 2026). `MAUI` is a modular framework that builds on a statistical emulator (in this case of `FASTWIND` synthetic spectra) with supervised machine-learning techniques and, coupled with MCMC sampling, enables a robust and efficient spectroscopic inference for massive star parameters and surface abundances. In particular, this subsample of stars has been specifically selected to cover the full range of T_{eff} , $\log g$, Y_{He} , and $v \sin i$ characterizing the complete sample analyzed with `IACOB-GBAT`. As illustrated in Fig. 2, the agreement of results between these two analysis approaches is also quite remarkable.

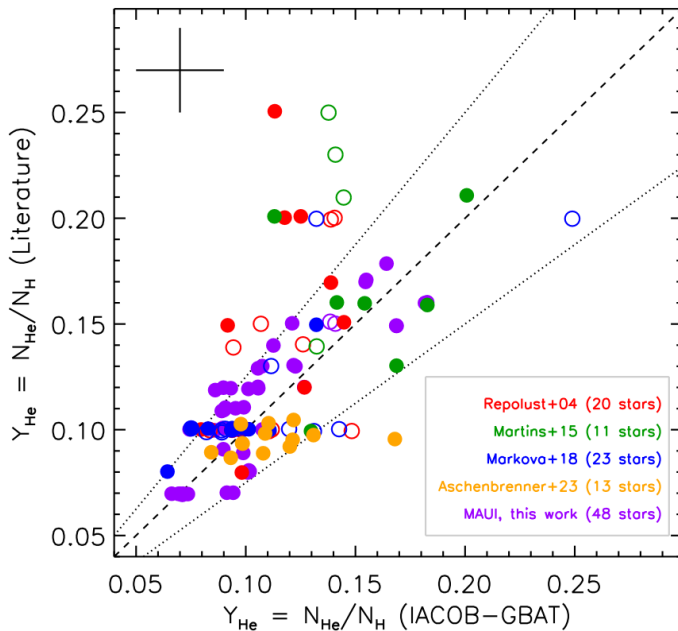


Fig. 2: Comparison of He abundances for a sample of 67 stars in common with the literature and 48 stars independently analyzed for this work using the code **MAUI**. Open symbols refer to stars for which we have provided a Q2 or Q3 quality flag to the **FASTWIND** fits (see Appendix C). The 1-to-1 relation and 25% tolerance region are shown as dashed and dotted lines, respectively. The cross at the top left corner indicates the typical uncertainties in the Y_{He} estimates.

4.3. The Hunter and spectroscopic HR diagrams

Figure 3 shows the distribution of the entire sample of stars in a modified version of the so-called Hunter diagram (c.f. Hunter et al. 2008), where the He abundance is used instead of nitrogen. Stars classified as ON or identified as SB1 and/or RWs are highlighted separately. For reference, we indicate in grey the main range of He abundances (mean value $\pm 2\sigma$) covered by stars in Group 1, and with grey dashed lines the step values in Y_{He} defining the grid of **FASTWIND** models incorporated into **IACOB-GBAT**. We also report the percentage of He-rich stars among the samples with a $v \sin i$ below and above 200 km s $^{-1}$, respectively. This somewhat arbitrary threshold has been adopted in several previous studies (e.g., de Mink et al. 2013; Ramírez-Agudelo et al. 2013; Holgado et al. 2022; Sana et al. 2022; Britavskiy et al. 2023; Carretero-Castrillo et al. 2025) to separate the main low- $v \sin i$ component from the high-velocity tail in the distribution of projected rotational velocities commonly found in O stars. Indeed, as proposed by de Mink et al. (2013), stars with $v \sin i$ exceeding this threshold are most likely the products of binary interaction – following mass-transfer or merger events – rather than massive stars formed in isolation with such rapid rotation.

Figure 4 presents the location of the stars in the three He abundance groups defined in Sect. 4.1 within a spectroscopic Hertzsprung–Russell diagram (sHRD, Langer & Kudritzki 2014). As in Fig. 4, ON, SB1 and RW stars are differentiated from the rest of the sample. For reference, we also show the position of the ZAMS and the evolutionary tracks computed with the **GENEC** code by Ekström et al. (2012) for an initial spin rate $v_{\text{ini}}/v_{\text{crit}} = 0.4$. Sections of the tracks where the surface He abundance reaches 1.3 times the initial abundance – due to internal transport processes implemented in the models, together with

Table 3: Summary of statistics of RWs and clearly detected SB1 systems in the full sample and the three subsamples of He-normal/rich/low stars defined in Sect. 4.1

Full sample	#	Runaways		SB1 systems		
		Yes	%	#	Yes	%
All	268	77	29 %	237	73	31 %
$v \sin i < 200$	219	58	26 %	187	62	33 %
$v \sin i \geq 200$	49	19	39 %	50	11	22 %
He-normal	#	Yes	%	#	Yes	%
All	167	40	24 %	141	46	33 %
$v \sin i < 200$	138	31	22 %	112	40	36 %
$v \sin i \geq 200$	29	9	31 %	29	6	21 %
He-rich	#	Yes	%	#	Yes	%
All	62	30	48 %	57	10	18 %
$v \sin i < 200$	46	20	44 %	41	8	20 %
$v \sin i \geq 200$	16	10	62 %	16	2	12 %
He-low	#	Yes	%	#	Yes	%
All	39	7	18 %	39	17	44 %
$v \sin i < 200$	35	7	20 %	34	14	41 %
$v \sin i \geq 200$	4	0	0 %	5	3	60 %

the progressive removal of the outer stellar layers by winds for stars above $\sim 30 M_{\odot}$ – are highlighted with dashed green lines. We note that the initial spin rate considered in these models is definitely too high when accounting from the results presented in Holgado et al. (2022), who proposed that the peak of the spin distribution at birth for O-type stars is most likely located at $v_{\text{ini}}/v_{\text{crit}} = 0.10 – 0.15$. However, we used these single star evolution tracks as reference to show a extreme case of surface enrichment due to rotational mixing (see further notes in Sect. 5.2)

4.4. Statistical properties of the runaway and SB1 samples

We have runaway classifications for 268 stars (84.3%) in our working sample of 318 objects, and sufficient multi-epoch spectroscopy⁶ to assess the SB1 status for 237 stars (74.5%). In combination with their locations in the Hunter and sHR diagrams (Figs. 3 and 4, respectively), we summarize the corresponding runaway and SB1 statistics for the full sample, as well as for subsamples defined by He abundance and $v \sin i$, in columns 2–4 and 5–7 of Table 3, respectively.

Complementing this information, we also find that He-rich stars are much more common among runaways: 39% of the RW sample (comprising 77 stars) are He-rich, compared to only 17% in the non-RW sample (191 stars). We also find that He-rich stars are less common among SB1 systems: they represent 14% of the 73 SB1 sample, compared to 28% among the 164 LS sample. In this regard, we remind that a certain percentage of stars identified as LS could indeed be merger products, disrupted binaries, or undetected SB1 systems (due to the still insufficient number of available epochs, or the difficulty to separate the effect of intrinsic variability from the orbital motion in a binary system where the amplitude of radial velocity variation is below 15–20 km s $^{-1}$, Simón-Díaz et al. 2024).

⁶ Three or more spectra.

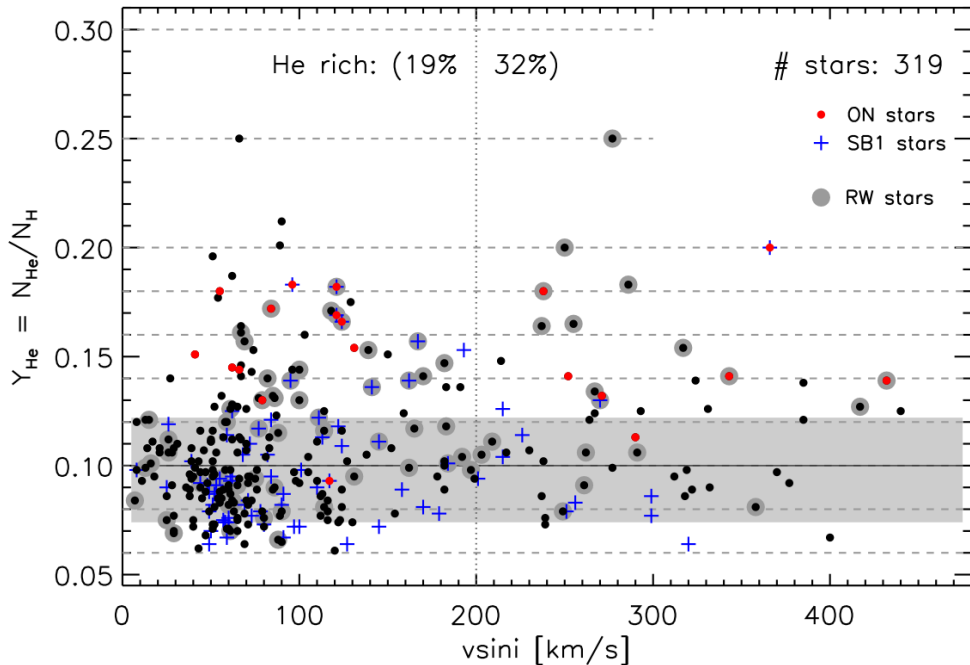


Fig. 3: Distribution of the 318 Galactic O-type stars in a modified Hunter diagram, using He abundance instead of nitrogen on the y-axis. The fractions of He-rich stars in the slow- and fast-rotating subsamples are indicated, assuming $v \sin i = 200 \text{ km s}^{-1}$ as the dividing threshold. ON, SB1 and RW stars are indicated with red small circles, blue crosses, and grey circles, respectively.

5. Discussion

5.1. The He-low sample

One of the first aspects that drew our attention was the non-negligible fraction of stars ($\sim 18\%$) for which the default IACOB-GBAT analysis yielded He abundances in the range $Y_{\text{He}} = 0.06 - 0.08$ (see Fig. 1). These values reach well below the lower limits of He abundances typically reported for Galactic early B-type stars (e.g., Lyubimkov 1975; Nieva & Przybilla 2012), our Sun (e.g., Serenelli & Basu 2010; Moharana et al. 2024), blue compact very metal-poor dwarf galaxies (e.g., Izotov et al. 1999), and interstellar medium estimates based on radio recombination line observations (e.g., Tsivilev & Krasnov 2023). Such determinations have often been regarded as representative of the primordial He abundance (Pagel 2000).

Given this context, it is natural to suspect that our low He abundance determinations are not physically meaningful, but rather result from limitations in the analysis. Potential contributors include incorrect estimates of microturbulence or wind properties, modeling issues in certain regions of parameter space (e.g., T_{eff} or $\log g$), and contamination from faint, unresolved companions whose continuum contribution can dilute the diagnostic He lines. To investigate these possibilities, we compared stars in Groups 2 (He-low) and 1 (He-normal) in terms of their location in the sHRD (Fig. 4) and their microturbulent velocities (ξ_t), as derived from the default IACOB-GBAT analysis. We also examined whether SB1 systems are overrepresented among He-low stars (Table 3).

These comparisons reveal no significant differences in ξ_t between the two groups. In particular, the fraction of He-low stars actually decreases with increasing microturbulence, which is the opposite of what would be expected if their abundances were being systematically underestimated due to overestimated ξ_t . Likewise, although Group 2 stars appear to cluster in a specific region of the sHRD (top panel in Fig. 4), that region also contains

stars with normal He abundances, making systematic modeling limitations an unlikely explanation. Moreover, the relative percentages of He-low stars are similar among targets with assigned quality flags Q1, Q2, and Q3 (Table C.1), again suggesting that modeling issues are not the primary cause of the anomalously low He abundances.

Altogether, these results leave as the most plausible explanation that many of the He-low stars are systems with undetected companions, for which the IACOB-GBAT analysis yields spuriously low abundances. In this regard, it is noteworthy that the fraction of SB1 systems is larger in the He-low group (44%) than in the He-normal one (33%). Indeed, formal tests based on synthetic spectra computed with FASTWIND – in which the diagnostic lines were diluted by only 10% – show that a similar IACOB-GBAT analysis to that performed here can easily underestimate the He abundance by 0.01 – 0.02 (Martínez-Sébastián et al., in prep.). These tests therefore support the hypothesis that undetected companions (possibly combined with minor modeling effects) are responsible for the low He abundances found in Group 2 stars.

5.2. The He-rich sample in the context of single star evolution

As illustrated in Fig. 1, the distribution of surface He abundances is characterized by: (1) a dominant component comprising $\sim 80\%$ of the sample (Groups 1 and 2), centered at $Y_{\text{He}} \approx 0.095$ and displaying a dispersion broadly consistent with the He abundance uncertainties of our analysis, and (2) an extended tail of clearly enriched stars (Group 3), accounting for $\sim 20\%$ of the sample, with abundances covering the range $Y_{\text{He}} \sim 0.12 - 0.25$.

Rotationally induced mixing has been considered for more than three decades as the most likely explanation for the occurrence of these He-rich stars, with the efficiency of this process predicted to increase with both initial mass and rotation rate. (e.g., Maeder & Meynet 2000; Heger & Langer 2000; Meynet & Maeder 2000; Brott et al. 2011; Ekström et al. 2012). How-

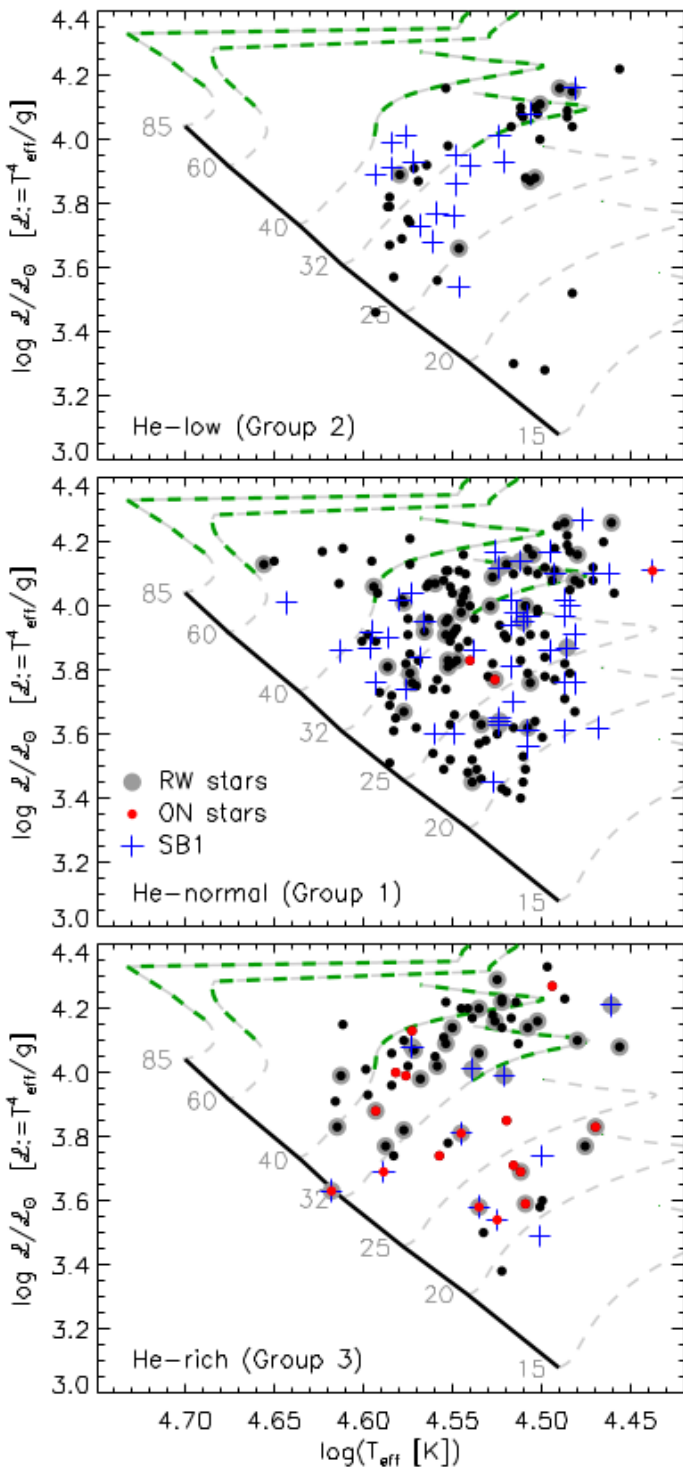


Fig. 4: Distribution of our sample of 318 Galactic O-type stars in a sHRD separated by the three He abundance groups described in Sect. 4.1. Evolutionary tracks from Ekström et al. (2012) for an initial spin rate $v_{\text{ini}}/v_{\text{crit}} = 0.4$ are depicted for reference purposes, highlighting in green the sections of the tracks where the He surface abundance reaches over 1.3 the initial abundance. Symbols are the same as in Fig. 3.

ever, we provide below two independent pieces of evidence indicating that this internal mixing mechanism alone cannot explain the observed distribution of stars under study in the $\text{He} - v \sin i$ and sHR diagrams presented in Figs. 3 and 4, respectively.

As in previous studies focusing on nitrogen (e.g. Hunter et al. 2008; Rivero González et al. 2012; Bouret et al. 2013; Grin et al. 2017), the $\text{He} - v \sin i$ diagram does not reveal a clear correlation between the two quantities. Indeed, there is a non-negligible number of He-rich stars with relatively low $v \sin i$. In addition, while the percentage of He-rich stars within the tail of fast-rotators is clearly larger than in the main low- $v \sin i$ component (32% vs. 19%, see Fig. 3), there is still a dominance of He-normal stars among the stars with $v \sin i > 200 \text{ km s}^{-1}$.

This long-standing issue has been extensively discussed in the literature (Brott et al. 2011; Maeder et al. 2014; Martins et al. 2017), where several effects have been proposed to partially account for the observed scatter when examining individual stars. For example, age may naturally explain the presence of some fast-rotating stars among the He-normal group, as they may simply be too young to display detectable abundance changes. This is evident from the evolutionary tracks shown in Fig. 4 where, even for stars born spinning at 40% of their critical velocity, only at the very end of the main sequence the He produced in the core is reaching the stellar surface to a detectable level. Similarly, the group of He-rich stars with low- $v \sin i$ could in principle be rapid rotators observed pole-on; however, this is unlikely given the large number of stars with these characteristics.

Focusing only on the $\text{He} - v \sin i$ diagram presented in Fig. 3, another plausible scenario might be that these He-rich, low $v \sin i$ objects provide observational evidence for efficient surface-braking mechanisms operating during the main-sequence phase, reducing the surface rotation rate while internal mixing continues to transport nuclear-processed material to the surface (see, e.g., Ekström et al. 2012). However, this proposal would be in tension with the observational findings by Holgado et al. (2022), de Burgos et al. (2024), and Nathaniel et al. (2025) about the non detection of a clear surface braking of massive stars along their main sequence evolution.

A more critical challenge to the rotational-mixing scenario arises from the distribution of He-rich stars in the sHRD. A substantial fraction of Group 3 stars ($\sim 47\%$, i.e., those located below $\log(L/L_\odot) \sim 4.0$) occupy regions of the diagram where the rotating GENEC tracks of Ekström et al. (2012) do not predict such levels of enrichment. This is clearly illustrated in the bottom panel of Fig. 4, where the segments of the evolutionary tracks reaching He abundances 1.3 times higher than the initial value (comparable with Group 3 stars) are marked with thick dashed green lines. Even these models – among the most efficient in producing surface enrichment (see Keszthelyi et al. 2022) – fail to reproduce the observed population. This tension is also further strengthened by the fact that most O-type stars are likely born with initial equatorial velocities below $0.2 v_{\text{crit}}$ (Holgado et al. 2022), making very rapid initial rotation an unlikely explanation for the He-rich stars.

These results provide strong evidence that rotational mixing alone cannot be the dominant driver of surface He enrichment in Galactic O-type stars. Instead, our findings reinforce the growing consensus that additional mechanisms – most notably binary interaction, as it will be shown in next sections – might play a central role in shaping the observed He-abundance distribution.

5.3. Some insights from binary evolution

A large percentage of massive O stars are commonly found to be part of binary or higher-order systems (e.g. Kobulnicky & Fryer 2007; Kobulnicky et al. 2014; Chini et al. 2012; Sana et al. 2013; Moe & Di Stefano 2017; Sana et al. 2025; Mahy et al. 2009, 2013; Barbá et al. 2017; Offner et al. 2023, Gamen et al. subm.).

Sana et al. (2012) indicated that more than 70% of all massive stars will exchange mass with a companion at some point of their lives, leading to a binary merger in one-third of the cases. These relatively recent findings have revived a long-standing concern in stellar astrophysics – namely, the importance of accounting for binary evolution when interpreting the observed properties of massive-star populations (see, e.g., reviews by Vanbeveren 1988, 1993, 2004; Vanbeveren & Mennekens 2017; Marchant & Bodensteiner 2024; Marchant 2026, and references therein).

Within this context, it is important to keep in mind that mass transfer and merger events can modify the spin rates and the surface chemical composition of the stars involved in the interaction (e.g., de Mink et al. 2013; Farmer et al. 2023; Menon et al. 2024; Jin et al. 2025). Moreover, binary-interaction products will often be observed as apparently single stars (de Mink et al. 2014). This will certainly be the case for merger remnants as well as runaway stars resulting from disrupted binaries following the supernova explosion of the initially more massive companion. But also for binary systems in which the post-mass-transfer donor becomes difficult to be detected, either directly in the optical spectrum or through radial velocity variations of the currently more massive and optically more luminous component, the mass gainer. Only under specific orbital configurations and mass ratios gravitationally bound systems will be detected as SB1.

Although a detailed comparison between our observational results and theoretical predictions for binary-interaction products lies beyond the scope of this work, it is still useful to briefly comment on the expected behavior of mass gainers from binary evolution models. Figure 5 depicts the distribution in the sHRD of a sample of mass gainers as predicted by computations performed by Jin et al. (2025). These authors have created a comprehensive grid of massive binary evolution models for solar metallicity computed with the MESA stellar evolution code (first introduced in Paxton et al. 2011). They covered a range of initial primary star masses from 5 to 100 M_{\odot} . Their computations incorporate detailed stellar and binary physics, including internal differential rotation, magnetic angular momentum transport, mass-dependent overshooting, stellar wind mass-loss, mass and angular momentum transfer and tidal interaction. Specifically, the outcome of their computations presented in Fig. 5 corresponds to the moment just after mass accretion and thermal relaxation has occurred, and before further nuclear-timescale evolution has taken place.

Within the full sample of resulting mass gainers, we highlight those with surface He abundances exceeding 1.2 times the initial value. This subsample is expected to correspond to the stars comprising Group 3, whose locations are shown again in Fig. 5 with open circles for reference. In this context, it is important to recall that the positions of the highlighted gainers (see also below) should be interpreted as their effective “birth” locations following the mass-transfer event. From these positions, all of these stars are expected to continue their subsequent main-sequence evolution toward lower effective temperatures.

From inspection of Fig. 5, and bearing in mind that helium-contaminated mass gainers are expected to remain He-rich throughout their subsequent evolution (Jin et al. 2025), we can draw a general conclusion. Binary interaction through mass-transfer events can naturally account for the presence of He-rich O-type stars in regions of the sHRD where rotating single-star evolutionary models fail to reproduce the observations (bottom panel of Fig. 4). In particular, the computations performed by Jin et al. (2025) indicate that strongly helium-enriched case A mass gainers (red filled circles) can readily reach the single-star ZAMS line before continuing their post mass-transfer evolution.

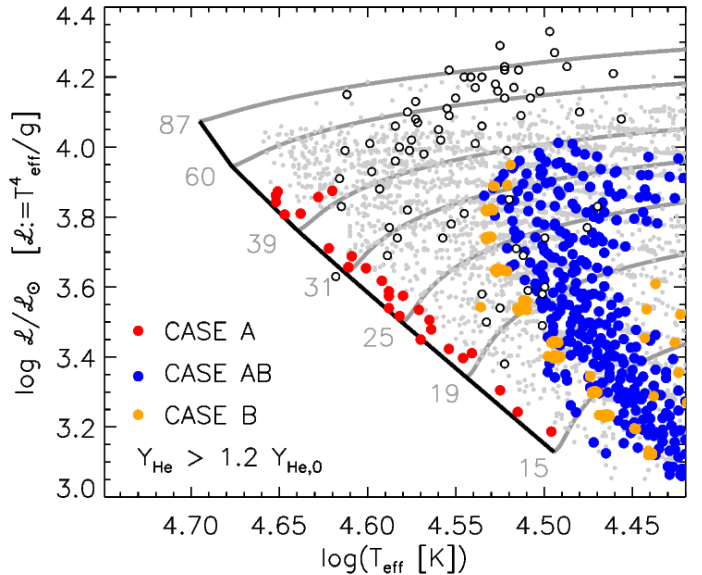


Fig. 5: Distribution in the sHRD of the birth location of mass gainers as predicted by the binary evolution computations by Jin et al. (2025). The full sample of gainers is depicted with gray colors, while those with enriched He abundances are highlighted with colors separating the mass-transfer cases A (red), B (orange) and AB (blue). Single star evolutionary tracks computed with the MESA stellar evolution code by Jin et al. (2024a) and used as basis for the binary evolution computation are also depicted for reference purposes. Open circles show the location of the He-rich group of O-type stars from our study.

These objects correspond to secondary stars from the highest mass binaries in the model grid, which only undergo fast case A mass transfer (see section 3.1.2 in Jin et al. 2025). In addition, He-rich gainers resulting from case B (orange) and AB (blue) mass-transfer can also populate the region of the sHRD under study. There is a gap between the ZAMS and their positions in the diagram because the secondaries are already significantly evolved by the time the primaries deplete core hydrogen and case AB or case B mass transfer occurs⁷.

A second conclusion that could be extracted is that the binary channel does not appear to operate efficiently at luminosities above $\log(\mathcal{L}/\mathcal{L}_{\odot}) \sim 4.0$. This would support a scenario in which the combined effects of rotationally induced mixing and wind-driven self-stripping in isolated stars become the dominant mechanisms responsible for surface He enrichment in stars occupying these regions of the sHRD (see also Fig. 4). Nevertheless, additional evolutionary pathways not represented in Fig. 5 may also contribute. For instance, in so-called reverse Algol systems (Sen et al. 2023), the donor star can remain the more luminous component of the binary, exhibit surface helium enrichment, and populate the upper part of the sHRD. Furthermore, a mass accretion efficiency is one of the most uncertain parameters in binary evolution, and a more efficient mass accretion than adopted in the models of Jin et al. (2025) can help populate the upper sHRD with helium-enriched mass gainers. Complementarily, although not explored here, merger events are also a viable explanation for some of the identified He-rich stars (Menon et al. 2024).

⁷ We note that if mass accretion was larger than assumed in the models computed by Jin et al. (2025), rejuvenation of this second set of gainers might be stronger and hence their birth location would be shifted towards the ZAMS line.

In this context, it is noteworthy that the fraction of stars with helium-enriched surfaces shows a clear dependence on (spectroscopic) luminosity. Below $\log(L/L_\odot) \sim 4.0$ – where neither rotational mixing nor wind stripping is expected to operate efficiently to enrich the surface with helium – the percentage of He-rich stars amounts to $\sim 16\%$. This percentage increases to $\sim 31\%$ at higher luminosities, where self-stripping by winds and rotational mixing becomes more effective in both single and binary stars.

5.4. The $Y_{\text{He}} - v \sin i$ diagram

The binary-evolution channel also introduces key elements for interpreting the distribution of O-type stars in the $Y_{\text{He}} - v \sin i$ diagram (Fig. 3), particularly in light of the shortcomings of the single star scenario (Sect. 5.2).

In systems undergoing case A mass transfer, the observed surface rotation of the He-rich gainer is not expected to exceed $\sim 200\text{--}250 \text{ km s}^{-1}$, because tidal forces efficiently counteract the spin-up induced by mass accretion (e.g. de Mink et al. 2013; Langer et al. 2020, and references therein). This could explain the non-negligible fraction of He-rich stars with $v \sin i < 200 \text{ km s}^{-1}$ (see Fig. 3 and Table 3). The same tidal effects may also explain for the relative scarcity of He-rich stars with very low projected rotational velocities ($v \sin i \lesssim 50 \text{ km s}^{-1}$). Additional channels – such as reverse-Algol systems, luminous wind-stripped single and binary stars, and stellar mergers – may also contribute to this population.

In case B (or AB) mass-transfer events, tidal forces are no longer sufficiently strong to prevent substantial spin-up of the gainer. Such interactions can therefore produce stars that simultaneously exhibit rapid rotation and – as shown in Sect. 5.3 – enhanced surface He abundances. Rotational mixing may also contribute to this population to some extent.

Finally, binary-evolution models predict that not all mass-transfer events lead to He-rich gainers (Jin et al. 2025). In addition, some pre-interaction binaries with low mass ratios may contribute to the He-normal population – in many cases, but not always, detected as SB1 systems – alongside stars evolving effectively as single.

Taken together, these effects naturally account for the coexistence of He-rich and He-normal stars across a wide range of projected rotational velocities and binary classifications, as observed in our sample.

5.5. Further insights from RWs and SB1 systems

Runaway stars provide valuable clues to identify past binary interactions. Their peculiar velocities are generally attributed to either the binary supernova scenario (BSS, Blaauw 1961) or to the dynamical ejection scenario (DES, Poveda et al. 1967). Among these channels, the BSS is particularly relevant for understanding the surface chemical properties of massive stars. Prior to the supernova (SN), mass transfer in the binary can spin up the future RW (the gainer) and modify its chemical composition, potentially leading to helium enrichment (Packet 1981; van den Heuvel 1985; Blaauw 1993). After the SN, the former binary will most likely result unbound, although not necessarily (e.g., Renzo et al. 2019; Carretero-Castrillo et al. 2025). These signatures – fast rotation, altered chemical abundances, and absence of detectable companions – are therefore expected in RW stars produced via binary interaction. In this context, assessing the RW and binarity status of He-rich O-type stars becomes an im-

portant diagnostic. As noted before, this work represents the first large-scale observational analysis combining He abundances, rotation, RW status, and SB1 information.

In Sect. 4.4 (see also Table 3 and Fig. 3), we showed that runaways are significantly more frequent among He-rich stars (48%) than among He-normal ones (24%), with the fraction increasing to 62% when considering only fast rotators. This result provides strong additional support for the binary-interaction scenario as the primary explanation for the presence of helium-enriched surfaces in a non-negligible fraction of O-type stars, and extends the conclusions reached by Britavskiy et al. (2023) and Carretero-Castrillo et al. (2025) in their studies of fast-rotating O-type stars.

Conversely, the fraction of detected SB1 systems is clearly lower in the He-rich sample (18%) compared to the He-normal population (33%). Several effects can account for this reduced SB1 incidence. As discussed above, a large fraction of He-rich stars are identified as runaways, suggesting that they are mass gainers in systems that underwent mass transfer – leading to helium enrichment – followed by disruption after the supernova explosion of the donor star (see Sect. 5.3). Consistent with this picture, only four out of the 30 He-rich runaway stars in our sample are detected as SB1 systems (Fig. 4).

In addition, a small fraction of He-rich stars may be merger products, in which any dynamical signature of binarity has been erased. Finally, some objects may correspond to post-mass-transfer systems that remain bound, but in which the initially more massive star has evolved into a low-mass stripped star or a compact object. In such cases, the donor becomes difficult to detect in the optical spectrum, while the mass gainer – the currently more massive and optically more luminous component – exhibits a relatively small orbital velocity amplitude, making SB1 detection particularly challenging. In this regard, the relatively low incidence of He-enrichment in the SB1s is consistent with the idea that binaries with significant radial velocity variations are mostly pre-interaction systems (de Mink et al. 2014).

5.6. The ON star sample

From basic stellar structure physics and single-star evolution, if the observed surface abundance pattern of H-burning CNO-cycle products in (main-sequence) O-type stars were solely the result of internal mixing, He-rich stars should also display a remarkable enhancement of nitrogen at their surfaces (see, e.g., Fig. 1 in Martínez-Sebastián et al. 2025). Although N abundances for the full sample of O-type stars considered in this work are not yet available (see, however Martínez-Sebastián et al. 2025, subm.), the ON qualifier used in spectral classification (Walborn 1970, 1971, 1976; Sota et al. 2011) can serve as a reliable proxy of such a strong N enrichment. These class of O-type stars were first identified by Walborn (1970) as having the nitrogen lines in their optical spectra considerably too strong for their spectral types, an anomaly which was postulated to be caused by abundance effects. This hypothesis was later confirmed by specific quantitative spectroscopic analyses (e.g., Schonberner et al. 1988; Martins et al. 2015b).

As noted in Sect. 2, our sample includes 19 ON stars, all of them highlighted in Figs. 3 and 4. Interestingly, while ON stars are not clearly separated from the rest of the population in terms of $v \sin i$ (Fig. 3), they show a strong tendency to be found among stars with surfaces enriched in helium. This confirms earlier findings by Martins et al. (2015b) based on a smaller dataset.

However, striking enough, the majority of He-rich stars ($\sim 80\%$) are not identified as ON. Once more, a piece of obser-

vational evidence that seems to indicate that rotationally-induced mixing might not be the dominant source of contamination of the stellar surfaces in a non-negligible fraction of O-type stars. We refer the reader to Martínez-Sebastián et al. (2025, subm.) for a more detailed investigation of this result incorporating information about N abundances in a subsample of the stars considered for this work.

6. Conclusions and future prospects

In this work we present strong observational evidence supporting the hypothesis that a large fraction of Galactic O-type stars – classified as apparently single or SB1 systems and presenting surfaces enriched in helium – are products of binary interaction.

Our conclusions are grounded in the first comprehensive and homogeneous quantitative spectroscopic analysis of He abundances in a statistically significant sample of Galactic O-type stars⁸. More than half of the stars identified as He-rich occupy regions of the sHRD that are clearly incompatible with the predictions of rotating single-star evolutionary models (even under the most efficient internal mixing assumptions; Ekström et al. 2012). By contrast, these locations can be naturally explained if these objects are mass gainers that have experienced a previous mass-transfer episode (or, in some cases, are the products of stellar mergers).

Binary-evolution models by Jin et al. (2025) predict that mass gainers resulting from case A, B, or AB mass-transfer events can reproduce the properties of the He-rich population found along the main-sequence band spanned by typical single O-type stars (~ 15 – $60 M_{\odot}$; see Fig. 5). Although not explored in detail here, some He-rich stars may also be reverse-Algol systems and merger products.

Additional observational clues reinforce this binary-interaction interpretation. The fraction of runaways is roughly a factor of two higher among He-rich stars compared to He-normal ones, while the fraction of detected SB1 systems is somewhat lower. Both trends qualitatively agree with expectations from binary evolution, where mass gainers may become runaways following a supernova explosion, or may lose their binary signature through mergers, unbound binaries, or through the presence of optically faint stripped companions (Blaauw 1961; de Mink et al. 2014).

As a consequence, surface He abundances therefore emerge as an efficient diagnostic to identify potential binary-interaction products, providing an accessible starting point for targeted follow-up observations. More broadly, the combination of T_{eff} , $\log g$, $v \sin i$, and He abundance measurements in statistically meaningful samples of O-type stars already offers valuable constraints for models of binary evolution and population synthesis. These constraints will become even more powerful when complemented with information on other chemical species (C, N, O), binary and runaway status, orbital parameters of SB1 systems (e.g., periods and radial velocity amplitudes, Gamen et al., subm.), and accurate stellar masses and luminosities (Holgado et al. 2025). The combination of all this observational information will also help to constraint to what extent the He-rich stars located above $\log(L/L_{\odot}) \sim 4.0$ are also the result of binary interaction, they are produced by a combination of rotationally-induced mixing and wind-stripping, or there is combination of various of these effects.

⁸ To our knowledge, this is the largest sample of stars of this type ever investigated in such detail.

From 318 Galactic O-type stars gathered by the IACOB project, we identified approximately 70 with clear helium enrichment, corresponding to $\sim 22\%$ of the sample. Among them, 11 are SB1 systems whose orbital properties warrant dedicated multiwavelenght follow-up. In this sense, our study represents an intermediate step between earlier analyses of Galactic O-type stars – typically limited to a few dozen objects – and the order-of-magnitude increase in sample size that will soon be enabled by upcoming large-scale spectroscopic surveys such as WEAVE (Jin et al. 2024b) and 4MOST (de Jong et al. 2019).

Finally, while this paper has focused primarily on helium, complementary work investigating N abundances for a subset of these stars (those with $v \sin i \lesssim 150 \text{ km s}^{-1}$) is presented in Martínez-Sebastián et al. (2025, subm.). Together, these studies pave the way for a new generation of observational constraints on massive-star evolution in both single and binary channels.

Acknowledgements. S.S.-D., G.H., C.M.-S. and A.H. acknowledge support from the State Research Agency (AEI) of the Spanish Ministry of Science and Innovation (MICIN) and the European Regional Development Fund, FEDER under grants LOS MÚLTIPLES CANALES DE EVOLUCIÓN TEMPRANA DE LAS ESTRELLAS MASIVAS/PRODUCTOS DE LA INTERACCION DE ESTRELLAS MASIVAS REVELADOS POR GRANDES SONDEOS ESPECTROSCOPICOS, with references PID2021-122397NB-C21 / PID2024-159329NB-C21. This project received the support from the “La Caixa” Foundation (ID 100010434) under the fellowship code LCF/BQ/PI23/11970035. MC-C, JMP, and MR acknowledge financial support from the State Agency for Research of the Spanish Ministry of Science and Innovation under grants PID2022-136828NB-C41/AEI/10.13039/501100011033/ERDF/EU, and PID2022-138172NB-C43/AEI/10.13039/501100011033/ERDF/EU, and through the Unit of Excellence María de Maeztu 2025-2029 award to the Institute of Cosmos Sciences (CEX2024-001451-M, MICIU/AEI/10.13039/501100011033). The project leading to this application has received funding from European Commission (EC) under Project OCEANS - Overcoming challenges in the evolution and nature of massive stars, HORIZON-MSCA-2023-SE-01, No G.A 101183150 Funded by the European Union. Views and opinions expressed are however those of the author(s) only and do not necessarily reflect those of the European Union or the European Research Executive Agency (REA). Neither the European Union nor the granting authority can be held responsible for them. This work has made use of data from the European Space Agency (ESA) mission Gaia (<https://www.cosmos.esa.int/\protect\relax\itshape{Gaia}>), processed by the Gaia Data Processing and Analysis Consortium (DPAC, <https://www.cosmos.esa.int/web/\protect\relax\itshape{relax}\itshape{Gaia}/dpac/consortium>). Funding for the DPAC has been provided by national institutions, in particular the institutions participating in the Gaia Multilateral Agreement. Based on observations made with the Nordic Optical Telescope, operated by NOTSA, and the Mercator Telescope, operated by the Flemish Community, both at the Observatorio del Roque de los Muchachos (La Palma, Spain) of the Instituto de Astrofísica de Canarias. Based on observations at the European Southern Observatory in programs 073.D-0609(A), 077.B-0348(A), 079.D-0564(A), 079.D-0564(C), 081.D-2008(A), 081.D-2008(B), 083.D-0589(A), 083.D-0589(B), 086.D-0997(A), 086.D-0997(B), 087.D-0946(A), 089.D-0975(A).

References

- Aerts, C., Molenberghs, G., Kenward, M. G., & Neiner, C. 2014, ApJ, 781, 88
- Aschenbrenner, P., Przybilla, N., & Butler, K. 2023, A&A, 671, A36
- Barbá, R. H., Gamen, R., Arias, J. I., et al. 2010, in Revista Mexicana de Astronomía y Astrofísica Conference Series, Vol. 38, Revista Mexicana de Astronomía y Astrofísica Conference Series, 30–32
- Barbá, R. H., Gamen, R., Arias, J. I., & Morrell, N. I. 2017, in The Lives and Death-Throes of Massive Stars, ed. J. J. Eldridge, J. C. Bray, L. A. S. McClelland, & L. Xiao, Vol. 329, 89–96
- Blaauw, A. 1961, Bull. Astron. Inst. Netherlands, 15, 265
- Blaauw, A. 1993, in Astronomical Society of the Pacific Conference Series, Vol. 35, Massive Stars: Their Lives in the Interstellar Medium, ed. J. P. Cassinelli & E. B. Churchwell, 207
- Bohannan, B., Abbott, D. C., Voels, S. A., & Hummer, D. G. 1986, ApJ, 308, 728
- Bouret, J. C., Hillier, D. J., Lanz, T., & Fullerton, A. W. 2012, A&A, 544, A67
- Bouret, J. C., Lanz, T., Martins, F., et al. 2013, A&A, 555, A1
- Bouret, J. C., Martins, F., Hillier, D. J., et al. 2021, A&A, 647, A134

Brinkman, H. E., Tkachenko, A., & Aerts, C. 2025, arXiv e-prints, arXiv:2507.20785

Britavskiy, N., Simón-Díaz, S., Holgado, G., et al. 2023, *A&A*, 672, A22

Brott, I., de Mink, S. E., Cantiello, M., et al. 2011, *A&A*, 530, A115

Carretero-Castrillo, M., Ribó, M., & Paredes, J. M. 2023, *A&A*, 679, A109

Carretero-Castrillo, M., Ribó, M., Paredes, J. M., et al. 2025, arXiv e-prints, arXiv:2510.21577

Cazorla, C., Nazé, Y., Morel, T., et al. 2017, *A&A*, 604, A123

Chini, R., Hoffmeister, V. H., Nasser, A., Stahl, O., & Zinnecker, H. 2012, *MNRAS*, 424, 1925

de Burgos, A., Simón-Díaz, S., Urbaneja, M. A., & Puls, J. 2024, *A&A*, 687, A228

de Jong, R. S., Agertz, O., Berbel, A. A., et al. 2019, *The Messenger*, 175, 3

de Mink, S. E., Cantiello, M., Langer, N., et al. 2009, *A&A*, 497, 243

de Mink, S. E., Langer, N., Izzard, R. G., Sana, H., & de Koter, A. 2013, *ApJ*, 764, 166

de Mink, S. E., Sana, H., Langer, N., Izzard, R. G., & Schneider, F. R. N. 2014, *ApJ*, 782, 7

Dufont, P. L., Evans, C. J., Lennon, D. J., & Hunter, I. 2020, *A&A*, 634, A6

Dufont, P. L., Thompson, A., Crowther, P. A., et al. 2018, *A&A*, 615, A101

Ekström, S., Georgy, C., Eggenberger, P., et al. 2012, *A&A*, 537, A146

Farmer, R., Laplace, E., Ma, J.-z., de Mink, S. E., & Justham, S. 2023, *ApJ*, 948, 111

Frischknecht, U., Hirschi, R., Meynet, G., et al. 2010, *A&A*, 522, A39

Gaia Collaboration, Brown, A. G. A., Vallenari, A., et al. 2016, *A&A*, 595, A2

Gaia Collaboration, Vallenari, A., Brown, A. G. A., et al. 2023, *A&A*, 674, A1

Gamen, R., Barbá, R. H., Morrell, N. I., Arias, J., & Maíz Apellániz, J. 2008, in *Revista Mexicana de Astronomía y Astrofísica Conference Series*, Vol. 33, *Revista Mexicana de Astronomía y Astrofísica Conference Series*, 54–54

Grin, N. J., Ramírez-Agudelo, O. H., de Koter, A., et al. 2017, *A&A*, 600, A82

Groenewegen, M. A. T., Lamers, H. J. G. L. M., & Pauldrach, A. W. A. 1989, *A&A*, 221, 78

Heger, A. & Langer, N. 2000, *ApJ*, 544, 1016

Herrero, A., Corral, L. J., Villamariz, M. R., & Martín, E. L. 1999, *A&A*, 348, 542

Herrero, A., Kudritzki, R. P., Vilchez, J. M., et al. 1992, *A&A*, 261, 209

Herrero, A., Puls, J., & Villamariz, M. R. 2000, *A&A*, 354, 193

Hillier, D. J. & Miller, D. L. 1998, *ApJ*, 496, 407

Holgado, G. 2019, PhD thesis, Astrophysical Institute of the Canaries; University of La Laguna, Spain

Holgado, G., Simón-Díaz, S., Barbá, R. H., et al. 2018, *A&A*, 613, A65

Holgado, G., Simón-Díaz, S., Haemmerlé, L., et al. 2020, *A&A*, 638, A157

Holgado, G., Simón-Díaz, S., & Herrero, A. 2025, *A&A*, 703, A175

Holgado, G., Simón-Díaz, S., Herrero, A., & Barbá, R. H. 2022, *A&A*, 665, A150

Hunter, I., Brott, I., Langer, N., et al. 2009, *A&A*, 496, 841

Hunter, I., Brott, I., Lennon, D. J., et al. 2008, *ApJ*, 676, L29

Izotov, Y. I., Chaffee, F. H., Foltz, C. B., et al. 1999, *ApJ*, 527, 757

Jin, H., Langer, N., Ercolino, A., & de Mink, S. E. 2025, arXiv e-prints, arXiv:2510.19965

Jin, H., Langer, N., Lennon, D. J., & Proffitt, C. R. 2024a, *A&A*, 690, A135

Jin, S., Trager, S. C., Dalton, G. B., et al. 2024b, *MNRAS*, 530, 2688

Keszthelyi, Z., de Koter, A., Götzberg, Y., et al. 2022, *MNRAS*, 517, 2028

Keszthelyi, Z., Meynet, G., Georgy, C., et al. 2019, *MNRAS*, 485, 5843

Keszthelyi, Z., Meynet, G., Martins, F., de Koter, A., & David-Uraz, A. 2021, *MNRAS*, 504, 2474

Keszthelyi, Z., Meynet, G., Shultz, M. E., et al. 2020, *MNRAS*, 493, 518

Kobulnicky, H. A. & Fryer, C. L. 2007, *ApJ*, 670, 747

Kobulnicky, H. A., Kiminki, D. C., Lundquist, M. J., et al. 2014, *ApJS*, 213, 34

Kudritzki, R. P., Simon, K. P., & Hamann, W. R. 1983, *A&A*, 118, 245

Kurucz, R. L. 1993, *Atomic Line Data*, Kurucz CD-ROM No. 2-12, Cambridge, MA: Smithsonian Astrophysical Observatory

Langer, N. 1992, *A&A*, 265, L17

Langer, N. & Kudritzki, R. P. 2014, *A&A*, 564, A52

Langer, N., Schürmann, C., Stoll, K., et al. 2020, *A&A*, 638, A39

Lyubimkov, A. S. 1975, *Astrophysics*, 11, 462

Maeder, A. 1987, *A&A*, 178, 159

Maeder, A. 1990, *A&AS*, 84, 139

Maeder, A. & Meynet, G. 2000, *ARA&A*, 38, 143

Maeder, A., Przybilla, N., Nieva, M.-F., et al. 2014, *A&A*, 565, A39

Mahy, L., Nazé, Y., Rauw, G., et al. 2009, *A&A*, 502, 937

Mahy, L., Rauw, G., De Becker, M., Eenens, P., & Flores, C. A. 2013, *A&A*, 550, A27

Maíz Apellániz, J., Alonso Moragón, A., Ortiz de Zárate Alcarazo, L., & GOSSS Team. 2017, in *Highlights on Spanish Astrophysics IX*, ed. S. Arribas, A. Alonso-Herrero, F. Figueiras, C. Hernández-Monteagudo, A. Sánchez-Lavega, & S. Pérez-Hoyos, 509–509

Maíz Apellániz, J., Pantaleoni González, M., Barbá, R. H., et al. 2018, *A&A*, 616, A149

Maíz Apellániz, J., Sota, A., Arias, J. I., et al. 2016, *ApJS*, 224, 4

Maíz Apellániz, J., Sota, A., Morrell, N. I., et al. 2013, in *Massive Stars: From alpha to Omega*, 198

Marchant, P. 2026, in *Encyclopedia of Astrophysics*, Vol. 2, 264–278

Marchant, P. & Bodensteiner, J. 2024, *ARA&A*, 62, 21

Markova, N., Puls, J., & Langer, N. 2018, *A&A*, 613, A12

Martínez-Sébastián, C., Simón-Díaz, S., Jin, H., et al. 2025, *A&A*, 693, L10

Martins, F., Bouret, J. C., Hillier, D. J., et al. 2024, *A&A*, 689, A31

Martins, F., Foschino, S., Bouret, J. C., Barbá, R., & Howarth, I. 2016, *A&A*, 588, A64

Martins, F., Hervé, A., Bouret, J. C., et al. 2015a, *A&A*, 575, A34

Martins, F., Simón-Díaz, S., Barbá, R. H., Gamen, R. C., & Ekström, S. 2017, *A&A*, 599, A30

Martins, F., Simón-Díaz, S., Palacios, A., et al. 2015b, *A&A*, 578, A109

Menon, A., Ercolino, A., Urbaneja, M. A., et al. 2024, *ApJ*, 963, L42

Meynet, G. & Maeder, A. 2000, *A&A*, 361, 101

Moe, M. & Di Stefano, R. 2017, *ApJS*, 230, 15

Moharana, S., Hema, B. P., & Pandey, G. 2024, *ApJ*, 974, 312

Mokiem, M. R., de Koter, A., Puls, J., et al. 2005, *A&A*, 441, 711

Mombarg, J. S. G., Varghese, A., & Ratnasingam, R. P. 2025, *A&A*, 695, A255

Morel, T., Hubrig, S., & Briquet, M. 2008, *A&A*, 481, 453

Nathaniel, K., Langer, N., Simón-Díaz, S., et al. 2025, *A&A*, 702, A197

Nieva, M. F. & Przybilla, N. 2012, *A&A*, 539, A143

Offner, S. S. R., Moe, M., Kratter, K. M., et al. 2023, in *Astronomical Society of the Pacific Conference Series*, Vol. 534, *Protostars and Planets VII*, ed. S. Inutsuka, Y. Aikawa, T. Muto, K. Tomida, & M. Tamura, 275

Packet, W. 1981, *A&A*, 102, 17

Pagel, B. E. J. 2000, *Phys. Rep.*, 333, 433

Paxton, B., Bildsten, L., Dotter, A., et al. 2011, *ApJS*, 192, 3

Poveda, A., Ruiz, J., & Allen, C. 1967, *Boletín de los Observatorios Tonantzintla y Tacubaya*, 4, 86

Proffitt, C. R., Jin, H., Daflon, S., et al. 2024, *ApJ*, 968, 1

Proffitt, C. R., Lennon, D. J., Langer, N., & Brott, I. 2016, *ApJ*, 824, 3

Przybilla, N., Firshtein, M., Nieva, M. F., Meynet, G., & Maeder, A. 2010, *A&A*, 517, A38

Puls, J., Kudritzki, R.-P., Herrero, A., et al. 1996, *A&A*, 305, 171

Puls, J., Urbaneja, M. A., Venero, R., et al. 2005, *A&A*, 435, 669

Ramírez-Agudelo, O. H., Simón-Díaz, S., Sana, H., et al. 2013, *A&A*, 560, A29

Renzo, M., Zapartas, E., de Mink, S. E., et al. 2019, *A&A*, 624, A66

Repolust, T., Puls, J., & Herrero, A. 2004, *A&A*, 415, 349

Richards, S., Eldridge, J., Ghodla, S., & Briel, M. 2024, arXiv e-prints, arXiv:2411.03000

Rivero González, J. G., Puls, J., & Najarro, F. 2011, *A&A*, 536, A58

Rivero González, J. G., Puls, J., Najarro, F., & Brott, I. 2012, *A&A*, 537, A79

Sabín-Sanjulán, C., Simón-Díaz, S., Herrero, A., et al. 2014, *A&A*, 564, A39

Sana, H., de Koter, A., de Mink, S. E., et al. 2013, *A&A*, 550, A107

Sana, H., de Mink, S. E., de Koter, A., et al. 2012, *Science*, 337, 444

Sana, H., Ramírez-Agudelo, O. H., Hénault-Brunet, V., et al. 2022, *A&A*, 668, L5

Sana, H., Shenar, T., Bodensteiner, J., et al. 2025, *Nature Astronomy*, 9, 1337

Santolaya-Rey, A. E., Puls, J., & Herrero, A. 1997, *A&A*, 323, 488

Schonberner, D., Herrero, A., Becker, S., et al. 1988, *A&A*, 197, 209

Sen, K., Langer, N., Pauli, D., et al. 2023, *A&A*, 672, A198

Serenelli, A. M. & Basu, S. 2010, *ApJ*, 719, 865

Simón-Díaz, S. 2020, in *Reviews in Frontiers of Modern Astrophysics: From Space Debris to Cosmology*, ed. P. Kabáth, D. Jones, & M. Skarka, 155–187

Simón-Díaz, S., Britavskiy, N., Castro, N., Holgado, G., & de Burgos, A. 2024, arXiv e-prints, arXiv:2405.11209

Simón-Díaz, S., Castro, N., Herrero, A., et al. 2011, in *Journal of Physics Conference Series*, Vol. 328, *Journal of Physics Conference Series*, 012021

Simón-Díaz, S., Godart, M., Castro, N., et al. 2017, *A&A*, 597, A22

Simón-Díaz, S., & Herrero, A. 2007, *A&A*, 468, 1063

Simón-Díaz, S., & Herrero, A. 2014, *A&A*, 562, A135

Simón-Díaz, S., Negueruela, I., Maíz Apellániz, J., et al. 2015, in *Highlights of Spanish Astrophysics VIII*, 576–581

Simón-Díaz, S., Pérez Prieto, J. A., Holgado, G., de Burgos, A., & Iacob Team. 2020, in *XIV.0 Scientific Meeting (virtual) of the Spanish Astronomical Society*, 187

Simoniello, R., Meynet, G., Ekström, S., Georgy, C., & Granada, A. 2015, in *IAU Symposium*, Vol. 307, *New Windows on Massive Stars*, ed. G. Meynet, C. Georgy, J. Groh, & P. Stee, 142–143

Song, H., Wang, J., Song, F., et al. 2018, *ApJ*, 859, 43

Sota, A., Maíz Apellániz, J., Morrell, N. I., et al. 2014, *ApJS*, 211, 10

Sota, A., Maíz Apellániz, J., Walborn, N. R., et al. 2011, *ApJS*, 193, 24

Tsviliev, A. P. & Krasnov, V. V. 2023, *Astronomy Reports*, 67, 250

Urbaneja, M. A. 2026, arXiv e-prints, arXiv:2601.01491

van den Heuvel, E. P. J. 1985, in *Birth and Evolution of Massive Stars and Stellar Groups*, ed. W. Boland & H. van Woerden, Vol. 120, 107

Vanbeveren, D. 1988, *Ap&SS*, 149, 1

Vanbeveren, D. 1993, *Space Sci. Rev.*, 66, 327

Vanbeveren, D. 2004, in *EAS Publications Series*, Vol. 13, *EAS Publications Series*, ed. M. Heydari-Malayeri, P. Stee, & J. P. Zahn (EDP), 141–161

Vanbeveren, D. & Mennekens, N. 2017, in *Astronomical Society of the Pacific Conference Series*, Vol. 508, *The B[e] Phenomenon: Forty Years of Studies*, ed. A. Miroshnichenko, S. Zharikov, D. Korčáková, & M. Wolf, 121

Villamariz, M. R., & Herrero, A. 2000, *A&A*, 357, 597

Villamariz, M. R., Herrero, A., Becker, S. R., & Butler, K. 2002, *A&A*, 388, 940

Voels, S. A., Bohannan, B., Abbott, D. C., & Hummer, D. G. 1989, *ApJ*, 340, 1073

Walborn, N. R. 1970, *ApJ*, 161, L149

Walborn, N. R. 1971, *ApJ*, 164, L67

Walborn, N. R. 1976, *ApJ*, 205, 419

Appendix A: IACOB-GBAT experiments to investigate the reliability of Y_{He} estimations

The IACOB-GBAT code provides the flexibility to perform a variety of controlled tests aimed at evaluating the impact of fixing selected fitting parameters or excluding specific diagnostic lines from the analysis. In the context of this study, we carried out three experiments of particular relevance.

The first one is motivated by the common practice in several previous spectroscopic studies of fixing the value of the microturbulent velocity (ξ_t) during the analysis. This approach was adopted, for example, by Martins et al. (2015a,b), who fixed ξ_t to 10 km s^{-1} in their formal solutions, independently of luminosity class. Similarly, Repolust et al. (2004) assumed $\xi_t = 10 \text{ km s}^{-1}$ for stars later than O6 and $\xi_t = 0 \text{ km s}^{-1}$ for earlier spectral types, again irrespective of luminosity class. In the same vein, Markova et al. (2018) fixed ξ_t to 10 km s^{-1} for mid- and late-O stars, while adopting a value of 15 km s^{-1} for hotter objects.

In this first experiment, we therefore repeated the IACOB-GBAT analysis using exactly the same set of diagnostic lines as in the default configuration, but fixing the microturbulence to $\xi_t = 10 \text{ km s}^{-1}$. The results are summarized in the top panels of Fig. A.1, which illustrate the impact of this assumption on the derived values of T_{eff} , $\log g$, $\log Q$, and Y_{He} . Specifically, the three leftmost panels explore possible correlations between changes in T_{eff} and $\log g$, Y_{He} , and ξ_t , and Y_{He} and $\log Q$, respectively, while the fourth panel shows a direct comparison between the He abundances obtained in the default IACOB-GBAT analysis and those resulting from this first experiment. In all panels, stars for which the difference in Y_{He} exceeds 25% are highlighted.

While the effects on the derived values of T_{eff} , $\log g$, and $\log Q$ are generally modest, a clear and expected correlation emerges between changes in ξ_t and Y_{He} (second panel from the left). In particular, we find a significant number of stars for which the He abundance increases by approximately 0.05 when adopting a fixed value of $\xi_t = 10 \text{ km s}^{-1}$ in the spectroscopic analysis, with a few cases showing even larger increases of $0.07 - 0.10$.

In the second experiment, we evaluated the impact of an incorrect determination of the wind-strength parameter, $\log Q$. This test was motivated by the identification of several tens of stars which we have labeled with quality flag Q2 in Tables C.1 to C.3 (see also Appendix C). In these stars, despite the overall good fitting found for all diagnostic lines, we detected indications of double-peaked emission affecting the wind-sensitive $\text{H}\alpha$ and $\text{He II} 4686$ lines.

To assess the potential effect of this issue, we repeated the IACOB-GBAT analysis while fixing the wind-strength parameter to $\log Q = -13.5$. This value corresponds to a relatively weak wind and provides a representative lower limit for the objects considered in this experiment.

The results of this experiment are presented in the second row of Fig. A.1, using a similar set of panels as in the case of the first experiment. Again, we found a non-negligible number of cases which will result in differences in Y_{He} larger than 25%. However, this will only happen when the difference in $\log Q$ is larger than 0.5 dex.

In the third and last experiment we explored what is the impact of excluding the two diagnostic lines which are more sensitive to microturbulence in this parameter domain: $\text{He I} 6678$ and $\text{He I} 5875$. These two lines are not so commonly used in other studies performing spectroscopic analyses of O-type stars, and we have found that, in the case of fast rotating stars, they seem to weight the best fitting solution (at least when using FASTWIND models) towards values of ξ_t in the range $20 - 30 \text{ km s}^{-1}$ (see

Appendix B), independently of the parameters of the stars. As a consequence, as described in the outcome of experiment 1, this could eventually have an impact in the derived He abundances, leading to somewhat lower estimates.

The results of this third experiment, presented in the last row of Fig. A.1, indicates that the impact of excluding the $\text{He I} 6678$ and $\text{He I} 5875$ diagnostic lines from the IACOB-GBAT analysis has a relatively small impact for about 90% of the stars in the sample. Only 35 stars (most of them fast rotators) show differences in the derived abundances above 25%. Interestingly, within this relatively small sample, it does not seem to be a clear correlation between modifications in the estimated Y_{He} and ξ_t , as illustrated by the second leftmost panel in the third row of Fig. A.1.

Overall, the main conclusion which can be extracted from these experiments is that there might be a small percentage of stars in our sample for which we could be obtaining too low He abundances. This underestimation should be, however, very occasionally larger than $\Delta Y_{\text{He}} \sim 0.05$.

Appendix B: Stars with discrepant He abundances

In Figure 4.2 we have presented a comparison of He abundance estimates obtained by means of the default IACOB-GBAT analysis (see Sect. 3) and those obtained in various previous studies in the literature. This sample amounts for a total of 61 stars, including 20, 11, 23 and 13 stars in common⁹ with Repolust et al. (2004); Martins et al. (2015b); Markova et al. (2018) and Aschenbrenner et al. (2023), respectively.

As described in Sect. 4.2, the overall agreement is quite good. However, there is a small subset of 14 stars for which we found discrepancies larger than 25%. All these stars are quoted in Table B.1, where we also provide several information of interest, as described in the corresponding caption.

Interestingly most of the highlighted stars have been labeled with a Q2 or Q3 quality flag (App. C). In addition, there is a quite remarkable number of them having a $v \sin i$ above 150 km s^{-1} .

We are aware that there are many additional affects which can be also contributing to the identified differences in derived He abundances (including, for example, the use of different spectra, some of them with poorer quality, as in the case of Repolust et al. 2004, or the use of different codes or diagnostic lines). However, after inspection of Table B.1, and taking into account the results of the experiments performed in Appendix A, the most likely explanation is connected with discrepancies between the microturbulences assumed by previous studies and the ones determined in our analysis.

Appendix C: Tables

Tables C.1, C.2, and C.3 summarize the relevant information of the 318 Galactic O-type stars analyzed in this study separated by the three groups of He abundances defined in Sect. 4.1. See introduction of Sect. 4 for further details.

Regarding column 10 (quality flag): Q1 refers to stars in which IACOB-GBAT provides a good agreement to all considered diagnostic lines; Q2 are stars for which a good quality fit is also obtained for all diagnostic lines, but the $\text{H}\alpha$ and/or $\text{He II} 4686$ lines seem to show some hits double peak emission affecting the wings of the line-profiles; lastly, the Q3 quality flag was assigned to those cases in which a simultaneous good fit to $\text{H}\alpha$ and $\text{He II} 4686$ is not fulfilled.

⁹ Note that some of the stars have been analyzed by several of the indicated authors.

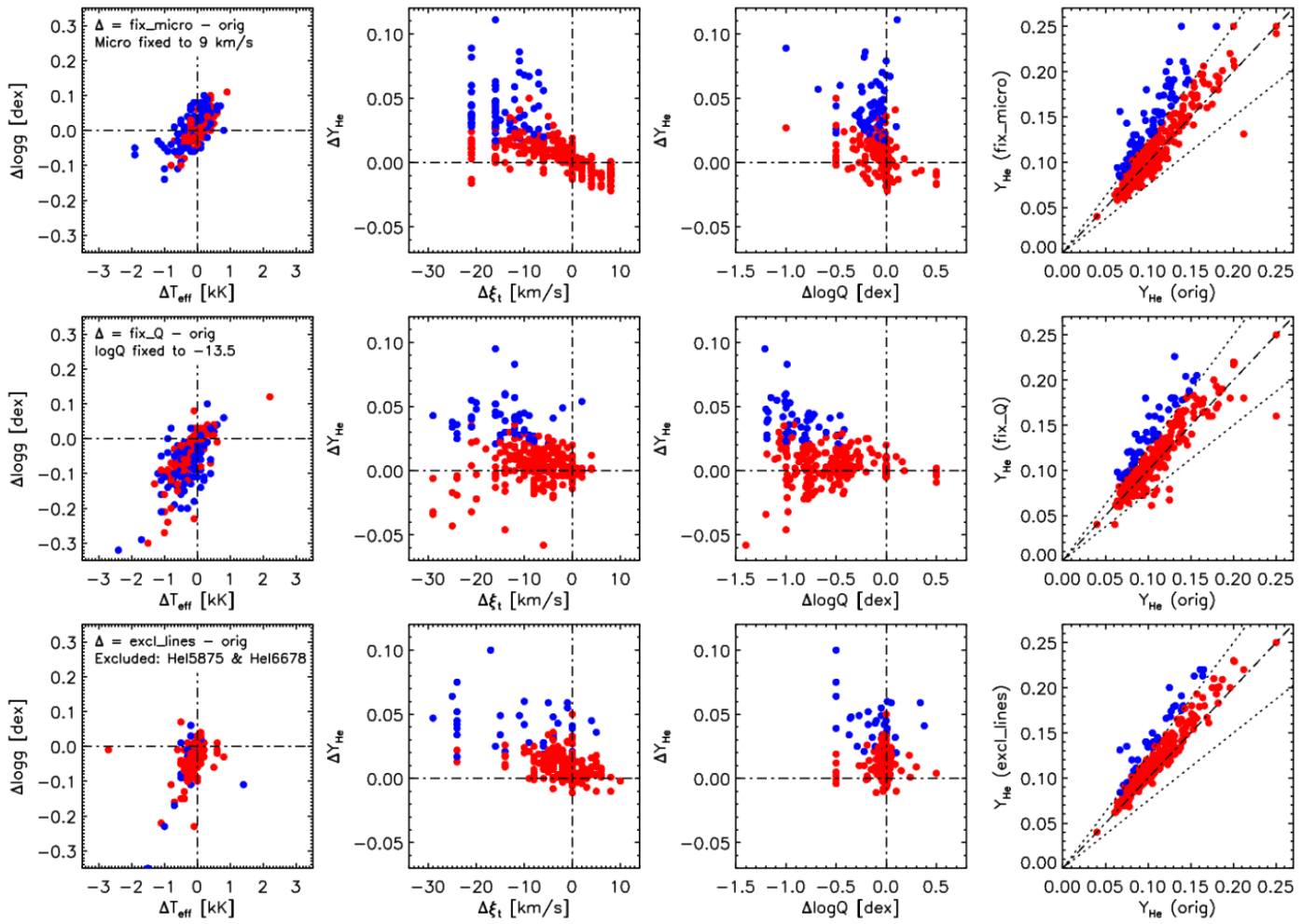


Fig. A.1: Study of the impact of certain assumptions in the IACOB-GBAT analysis

Table B.1: Stars in common with several studies in the literature for which we obtain discrepancies larger than 25% in the estimated He abundances. We also indicate the SpC, SB status and $v \sin i$ of the stars, as well as the T_{eff} and $\log g$ values obtained with the default IACOB-GBAT analysis (see Sect. 3 and those quoted in the reference studies (indicated in the last column). The table is complemented with the quality flag assigned to each of the IACOB-GBAT analyses (see App. C and the estimated value of microturbulence. In the case of the reference studies, this parameter was fixed to $\xi_t = 10$ and 15 km s^{-1} for the case of dwarfs/giants and supergiants, respectively, by Repolust et al. (2004, R04) and Markova et al. (2018, M18), and to $\xi_t = 10 \text{ km s}^{-1}$ by (Martins et al. 2015b, M15b). The microturbulence derived by Aschenbrenner et al. (2023, A23) for HD 14633 was 6 km s^{-1} .

ID	SpC	This work				Literature				SB status	Ref.
		$v \sin i$ [km s $^{-1}$]	T_{eff} [kK]	$\log g$ [dex]	ξ_t [km s $^{-1}$]	Y_{He}	Y_{He}	T_{eff} [kK]	$\log g$ [dex]		
HD 14947	O4.5 If	114	37.8	3.58	7	0.12	0.20	37.5	3.48	Q1	LPV
HD 193682	O4.5 IV(f)	183	39.3	3.68	9	0.12	0.20	40.0	3.65	Q1	LS
HD 210839	O6.5 Iab:(n)fp	214	36.3	3.50	30	0.15	0.10	36.0	3.58	Q2	LS
HD 192639	O7.5 Iabf	82	34.3	3.38	30	0.14	0.20	35.0	3.47	Q3	.
HD 24912	O7.5 III(n)((f))	230	35.7	3.51	25	0.11	0.15	35.0	3.56	Q2	LS
HD 217086	O7 Vnn((f))z	377	37.5	3.69	17	0.09	0.15	36.0	3.72	Q1	LS
HD 13268*	ON8.5 IIIn	290	34.7	3.61	25	0.11	0.25	33.0	3.48	Q1	LS
HD 18409	O9.7 Ib	131	30.2	3.11	21	0.09	0.14	30.0	3.04	Q2	LS
HD 191423*	ON9 II-IIIInn	432	32.5	3.46	25	0.14	0.20	32.5	3.60	Q2	LS
HD 13268*	ON8.5 IIIIn	290	34.7	3.61	25	0.11	0.20	32.0	3.63	Q1	LS
HD 150574	ON 9III(n)	252	33.1	3.51	20	0.14	0.23	31.0	3.49	Q2	MD
HD 191423*	ON9 II-IIIInn	432	32.5	3.46	25	0.14	0.20	31.5	3.72	Q2	LS
HD 123008	ON 9.2Iab	62	31.2	3.17	30	0.14	0.21	30.0	3.10	Q3	.
HD 69464	O7 Ib(f)	73	35.8	3.38	25	0.14	0.10	36.0	3.51	Q3	LS
HD 148546	O9 Iab	85	31.8	3.24	30	0.13	0.20	31.0	3.22	Q3	LS
HD 14633	ON 8.5V	121	35.1	3.80	9	0.17	0.10	34.0	3.9	Q1	SB1
											A23

Table C.1: Spectroscopic parameters for the sample analyzed in this work and identified as He-low.

Columns include: star ID; spectral classification (SpC) from the ALS catalog; projected rotational velocity ($v \sin i$) and macroturbulence (v_{mac}) derived with the IACOB-BROAD tool; a series of parameters obtained from the IACOB-GBAT/FASTWIND analysis including effective temperature (T_{eff}) and spectroscopic luminosity (Langer & Kudritzki 2014); Helium abundance (Y_{He}); microturbulence (ξ_1) and log Q. This information is complemented with a quality flag considering the fit of the FASTWIND model, the number of spectra available, as well as the spectroscopic binarity (SB) and runaway (RW) status of each target.

STAR-ID	SpC	$v \sin i$ [km s $^{-1}$]	v_{mac} [km s $^{-1}$]	T_{eff} [kK]	logLsp [dex]	YHe [dex]	micro. [km s $^{-1}$]	logQ [dex]	Qual. flag	sp	SB status	RW status
BD +453216A	O5 V((f))z	69	57	36.2 ± 0.8	3.56 ± 0.10	0.06 ± 0.01	1	-13.5	Q1	4	LPV	.
CPD -592600	O6 V((f))	127	106	39.2 ± 1.1	3.89 ± 0.13	0.06 ± 0.01	11	-12.7	Q1	8	SB1	NO
...
HD 124314	O6 IV(n)((f))	256	0	37.3 ± 0.8	3.93 ± 0.07	0.08 ± 0.01	17	-12.6	Q2	15	SB1	NO
HD 76556	O6 IV(n)((f))p	239	0	38.6 ± 0.9	3.79 ± 0.11	0.07 ± 0.01	25	-12.6	Q2	4	LS	NO
...
HD 152723	O6.5 III(f)	73	100	37.7 ± 0.7	4.01 ± 0.06	0.08 ± 0.01	5	-12.7	Q1	13	SB1	.
HD 156738	O6.5 III(f)	65	103	37.3 ± 1.0	3.91 ± 0.13	0.07 ± 0.02	15	-12.9	Q1	2	.	NO
...
HD 101205	O7 II:(n)	320	0	36.2 ± 0.8	3.77 ± 0.07	0.06 ± 0.01	11	-12.5	Q2	3	SB1	.
HD 100444	O9 II	52	77	32.5 ± 0.7	4.10 ± 0.08	0.07 ± 0.01	23	-12.7	Q1	3	LS	NO
...
HD 209975	O9 Ib	63	77	31.9 ± 0.3	4.10 ± 0.05	0.08 ± 0.01	21	-12.8	Q1	80	LS	NO
HD 155756	O9 Ibp	62	99	31.7 ± 0.5	4.11 ± 0.05	0.08 ± 0.01	25	-12.5	Q1	2	.	YES
...

SB status: **LS**: Likely single, **LPV**: Line profile variable, **SB1**: Single-lined spectroscopic binary.
Classifications based on fewer than three spectra (as indicated in the sp. column) should be treated with caution.

Table C.2: Spectroscopic parameters for the sample analyzed in this work and identified as He-normal.

Same columns as Table C.1

STAR-ID	SpC	$v \sin i$ [km s $^{-1}$]	v_{mac} [km s $^{-1}$]	T_{eff} [kK]	logLsp [dex]	YHe [dex]	micro. [km s $^{-1}$]	logQ [dex]	Qual. flag	sp	SB status	RW status
HD 64568	O3 V((f*))z	75	53	47.2 ± 1.8	0.00 ± 0.00	0.09 ± 0.02	30	-12.8	Q1	6	LS	YES
HD 93128	O3.5 V((fc))z	58	56	48.1 ± 2.5	0.00 ± 0.00	0.10 ± 0.03	25	-12.7	Q1	3	LS	NO
...
HD 193682	O4.5 IV(f)	183	90	39.3 ± 1.3	4.06 ± 0.09	0.12 ± 0.03	9	-12.7	Q1	5	LS	YES
HD 14434	O5.5 IVnn(f)p	417	0	38.6 ± 1.3	3.81 ± 0.12	0.13 ± 0.03	30	-12.9	Q2	6	LS	YES
...
HD 93250	O4 III(fc)	70	84	44.7 ± 1.5	4.14 ± 0.11	0.11 ± 0.02	30	-12.5	Q1	5	LS	NO
HD 93843	O5 III(fc)	58	120	37.5 ± 0.8	4.21 ± 0.03	0.12 ± 0.03	12	-12.5	Q3	5	LS	NO
...
HD 152233	O6 II(f)	62	105	37.4 ± 0.8	4.04 ± 0.08	0.12 ± 0.03	15	-12.5	Q3	54	SB1	NO
HD 157857	O6.5 II(f)	114	69	36.3 ± 0.8	4.07 ± 0.09	0.12 ± 0.02	17	-12.5	Q2	9	LS	YES
...
HD 15570	O4 If	81	115	40.9 ± 1.6	4.18 ± 0.10	0.10 ± 0.02	30	-11.9	Q1	8	LS	NO
HD 193514	O7 Ib(f)	73	84	35.6 ± 0.8	4.06 ± 0.10	0.08 ± 0.02	20	-12.5	Q3	4	LS	NO
...

SB status: **LS**: Likely single, **LPV**: Line profile variable, **SB1**: Single-lined spectroscopic binary.

Classifications based on fewer than three spectra (as indicated in the sp. column) should be treated with caution.

Table C.3: Spectroscopic parameters for the sample analyzed in this work and identified as He-rich.

Same columns as Table C.1

STAR-ID	SpC	$v \sin i$ [km s $^{-1}$]	v_{mac} [km s $^{-1}$]	T_{eff} [kK]	logLsp [dex]	YHe [dex]	micro. [km s $^{-1}$]	logQ [dex]	Qual. flag	sp	SB status	RW status
HD 256725	O5 V((fc))z	67	38	41.3 ± 1.4	3.91 ± 0.15	0.15 ± 0.05	9	-13.1	Q1	4	LS	NO
BD +60134	O5.5 V(n)((f))	250	0	41.2 ± 1.7	3.83 ± 0.20	$>0.20 \pm 0.07$	18	-13.0	Q1	4	LS	YES
...
HD 192281	O4.5 IV(n)(f)	277	0	41.0 ± 1.3	3.99 ± 0.09	$>0.25 \pm 0.07$	10	-12.8	Q2	9	LS	YES
HD 63005	O6.5 IV	56	66	38.4 ± 1.7	3.96 ± 0.19	0.13 ± 0.05	19	-13.1	Q1	2	.	NO
...
HD 338931	O6 III(f)	170	0	38.7 ± 1.4	3.77 ± 0.10	0.14 ± 0.04	25	-12.5	Q1	3	LS	YES
HD 190864	ON6.5 III(f)	66	90	37.4 ± 0.8	4.13 ± 0.08	0.14 ± 0.02	23	-12.8	Q1	4	LS	NO
...
HD 228368	O7 II	267	0	34.3 ± 1.4	4.06 ± 0.12	0.13 ± 0.05	30	-12.6	Q2	1	.	YES
HD 34656	O7.5 II(f)	67	77	35.9 ± 0.5	4.11 ± 0.03	0.16 ± 0.03	21	-12.7	Q1	111	LS	.
...
HD 190429A	O4 If	90	113	40.9 ± 1.7	4.15 ± 0.14	0.21 ± 0.07	30	-11.9	Q1	4	LS	NO
HD 14947	O4.5 If	114	22	37.8 ± 1.0	4.10 ± 0.10	0.12 ± 0.02	7	-12.1	Q1	4	LPV	.
...

SB status: **LS**: Likely single, **LPV**: Line profile variable, **SB1**: Single-lined spectroscopic binary.

Classifications based on fewer than three spectra (as indicated in the sp. column) should be treated with caution.